

Electrical Control of Anisotropic Ferromagnetic Domains During Antiferromagnetic-Ferromagnetic Phase Transition

X.Z. Chen,¹ H. Liu,² L.F. Yin,² C. Song,^{1,*} Y.Z. Tan,¹ X.F. Zhou,¹ F. Li,¹ Y.F. You,¹ Y.M. Sun,¹ and F. Pan^{1,†}

¹Key Laboratory of Advanced Materials (MOE), School of Materials Science and Engineering, Tsinghua University, Beijing 100084, China

²State Key Laboratory of Surface Physics and Department of Physics, Fudan University, Shanghai 200433, China

(Received 29 May 2018; revised manuscript received 11 October 2018; published 8 February 2019)

Current-driven motion of ferromagnetic domain walls has attracted intensive attention due to its rich physics and the potential applications in racetrack nonvolatile memory. However, the interplay between antiferromagnetic-ferromagnetic (AFM-FM) phase boundaries and current has remained elusive. Here, electrical control of anisotropic FM domains is investigated in AFM domains during the AFM-FM phase transition of Pd-doped FeRh films. For the as-grown state, the AFM-FM phase boundaries are initially aligned along the [100] axis with weak anisotropy. A stronger anisotropy is introduced by applying a current with a density of approximately 10^6 A/cm^2 . Moreover, the phase boundaries can be reversibly oriented by the applied (writing) current, giving rise to an orthogonal alignment between the phase boundaries and the current. Alignments of anisotropic FM domains generate multilevel resistance. Overall, the results confirm electrical control of domains in magnets, and provide an alternative way to create multilevel memories.

DOI: 10.1103/PhysRevApplied.11.024021

I. INTRODUCTION

Rotation or propagation of magnetic domains is generally involved in magnetization. Switching of individual nanoscale magnetic elements, such as tunnel junctions, has been used to build alternative magnetic memory and logic devices. Motion of domain walls (DWs) that is driven by a large current in a magnetic racetrack provides “racetrack memory” as alternative information storage that would innately be three-dimensional memory [1,2]. Thus, DWs’ motion has attracted extensive interest. A series of ferromagnetic films have been used, from simple FePd and Co films to (Ga,Mn)As single layers and perpendicular Co/Pt magnetized stacks [3–6]. Corresponding mechanisms such as spin-transfer torque and spin-orbit torque [7] have been attributed for DW motion. Relevant DWs were characterized by magnetic force microscopy (MFM) [8,9] and photoemission electron microscopy combined with x-ray magnetic circular dichroism [10,11].

In addition to ferromagnetic (FM) DWs, antiferromagnetic (AFM) DWs have been investigated for anti-ferromagnetic spintronics [12–16]. AFM domains of CuMnAs have been realigned by applied current via spin-orbit torque because of its oppositely arranged spin

sublattice [17]. Here, we propose that an alternative DW-like structure, the antiferromagnetic-ferromagnetic (AFM-FM) phase boundaries (PBs), are expected to be manipulated by the applied current, providing a unique opportunity to encode information. FeRh exhibits a first-order AFM to FM phase transition driven by temperature or a magnetic field [18,19], making it a possible candidate for the investigation of AFM-FM PBs and electrical control of AFM-FM PBs during the phase transition [20–24]. The AFM-FM PBs of Pd-doped FeRh films are initially aligned along the [100] axis with a weak anisotropy [25], which can be substantially stabilized along the [100] and rotated to the [010] axis by current applied along the [010] and [100] axes, respectively. The alignments of AFM-FM PBs are dependent on the magnitude of the applied current, which serves as a basis for multibit data storage.

II. METHODS

Pd-doped 30-nm-thick (1 at. %) FeRh (Pd-FeRh) films are grown on (001)-oriented single-crystal MgO substrates with dc magnetron sputtering [26]. Pd doping lowers the FeRh transition temperature to room temperature [27,28]. The base pressure is 2×10^{-5} Pa, and the films are deposited at 573 K and 0.8 Pa Ar pressure from a stoichiometric $\text{Fe}_{50}\text{Rh}_{50}$ target with a thin Pd rod, resulting in stoichiometric $\text{Fe}_{49.5}\text{Rh}_{49.5}\text{Pd}_1$ films. The films are then heated *in situ* to 1023 K and annealed for 100 min. Finally,

*songcheng@mail.tsinghua.edu.cn

†panf@mail.tsinghua.edu.cn

they are fabricated into an eight-terminal Hall cross by electron beam lithography and ion milling etching.

The microstructure of the Pd-FeRh films is analyzed with an x-ray diffractometer (XRD) using Cu K_{α} radiation. Transport measurements are performed with a Physical Property Measurement System that provides magnetic fields up to 9 Tesla (T) and variable temperatures over 1.5–400 K. MFM images are recorded with an Attocube system at 300 K and 9 T. Two-dimensional (2D) finite-element analysis is performed by COMSOL Multiphysics to simulate electrical scattering induced by the anisotropic FM domains. For this simulation, MFM images are first converted to binary ones, followed by edge detection in MATLAB, during which points on the PBs are extracted and imported directly into the geometry configuration [29]. The geometry of the eight-terminal Hall cross used for simulations is set proportional to the experimental devices, and the electrical scattering center is then introduced into the Hall cross based on the extracted PBs. The scattering centers refer to the FM-phase regions embedded inside the AFM matrix. Because of the different resistivities of the FM ($65 \mu\Omega \text{ cm}$) and AFM ($155 \mu\Omega \text{ cm}$) phases, a distorted electric field will be induced in the Hall cross, leading to the different voltages on the Hall arms.

III. RESULTS

The strong XRD peaks in Fig. 1(a) reflect the high quality of the Pd-FeRh films, with the Pd-FeRh (001) plane parallel to the MgO (001) substrates. The quality of the chemical ordering can be calculated by the order parameter S , $S = \sqrt{I_{001}^{\exp}/I_{002}^{\exp}}/1.07$, where I_{001}^{\exp} and I_{002}^{\exp} are the

intensities of the (001) and (002) Bragg reflections, respectively. The $S = 0.89$ result from Fig. 1(a) indicates high quality Pd-FeRh films. The films are then patterned on the Hall bar, which reveals the first-order transition from the AFM state (high-resistive state, HRS) to the FM state (low-resistive state, LRS), driven by the magnetic field ($\rho_{xx}-\mu_0 H$) at room temperature. The AFM and FM states coexist in the magnetic phase transition area, as indicated in Fig. 1(b); that is, 5.5–8.5 T for the AFM-FM transition and 4–1 T for the FM-AFM transition. Figure 1(c) is a schematic of the transport measurements, where ρ_{xx} and ρ_{xy} of the Pd-FeRh are denoted. The x -axis is along the [110] direction, while the y -axis is along the [110] orientation.

The symmetries of the Hall signals in the eight-terminal Hall cross during magnetic phase transitions of the Pd-FeRh films are determined via experiments depicted in Fig. 2(a) and are performed as follows. A small reading current of $100 \mu\text{A}$ is applied along the [010], [110], [100], and [110] axes of the Pd-doped FeRh films and the voltage is recorded in the vertical direction. The current direction in each measurement configuration is indicated in Fig. 2(a). The MFM image at left (magnified by a factor of two) reveals the coexistence of AFM and FM domains at 7 T, highlighted by the dashed square at the Hall cross. The corresponding field-dependent Hall resistivity is plotted at right as the ascending [Fig. 2(b)] and descending [Fig. 2(c)] branches of the magnetic-field-dependent resistivity curves (marked as curves I to IV and from I' to IV'). There are two eminent features in Fig. 2(b): (i) With increasing field, the polarity of the Hall signals undergoes the

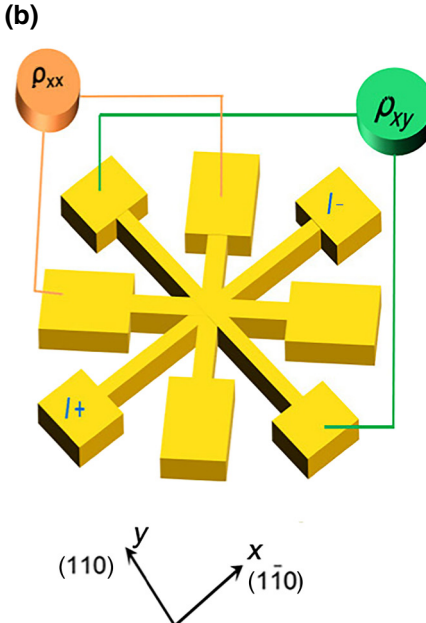
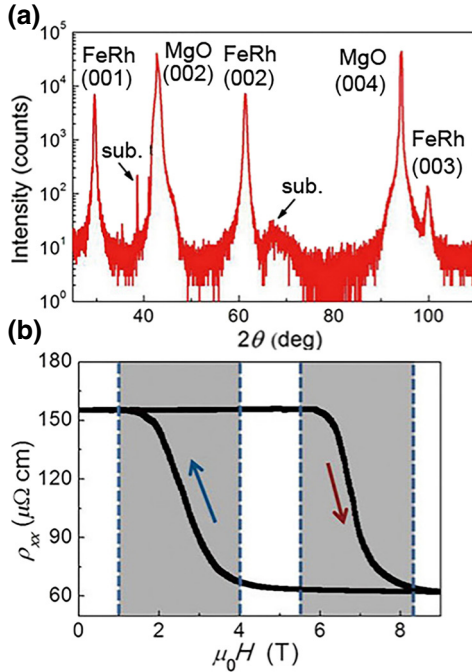


FIG. 1. (a) X-ray diffraction patterns of Pd-FeRh. (b) Resistivity of Pd-FeRh vs magnetic field from 0 to 9 T. The regions during the magnetic phase transition are denoted in a dark color. The AFM-FM and FM-AFM transitions are indicated with the red and blue arrows, respectively. (c) Schematics of the transport measurements of Pd-FeRh.

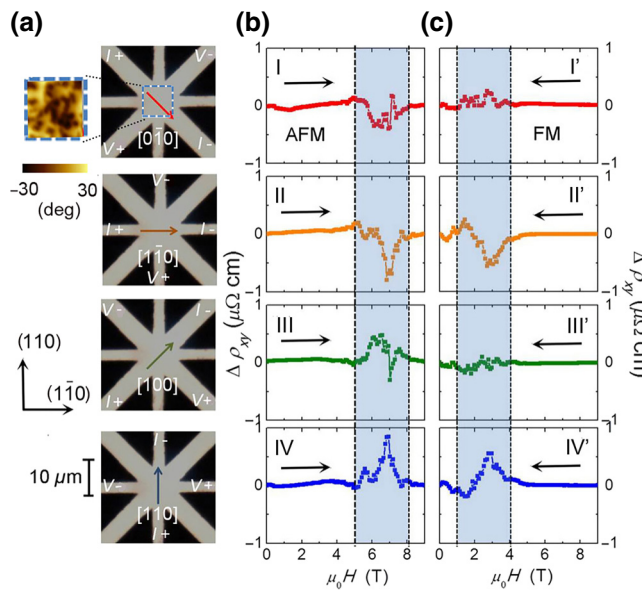


FIG. 2. (a) Schematics of Hall detection of anisotropic ferromagnetic domains in antiferromagnetic domains during the magnetic phase transition. The eight-terminal Hall cross is shown in the microscopic images. The MFM image (magnified by two times) shows the magnetic contrast of the dashed square of the Hall cross at 7 T. The reading current is applied along four different axes, that is, $[0\bar{1}0]$, $[\bar{1}\bar{1}0]$, $[100]$, and $[\bar{1}10]$ of Pd-FeRh, indicated by the arrows. The current directions are listed from top to bottom. The dashed square marks the region where MFM images are taken. The scale bar is $10 \mu\text{m}$ in length. (b) Hall evolutions when increasing the magnetic field from 0 to 9 T in different detecting geometries. (c) Hall evolutions when decreasing the magnetic field from 9 T to 0. The AFM-FM and FM-AFM phase transition regions are marked in blue. The resistivity-vs-field plots illustrated on the right in (b) and (c) correspond to the same current orientation as described on the left in (a).

variation of zero-negative-positive-zero, zero-negative-zero, zero-positive-negative-zero, and zero-positive-zero, as displayed from the top to the bottom panels, respectively; (ii) the absolute values of the Hall signals with only one polarity are larger than those with two polarities. The Hall signals exhibit a single but opposite polarity when the current flows along the $[\bar{1}\bar{1}0]$ and $[\bar{1}10]$ directions, indicating that the PBs of the Pd-doped FeRh films are aligned along the $[100]$ axis with a weak anisotropy. In this scenario, when the reading current is applied along the $[0\bar{1}0]$ and $[100]$ directions, the electrons are scattered randomly without apparent orientation, giving rise to both positive and negative Hall signals with smaller intensities. Similar but reduced Hall signals are observed for the FM-AFM transition in Fig. 2(c) when decreasing the magnetic field. This indicates that the AFM-FM PBs are aligned along the $[100]$ axis in the reciprocal process.

Large current pulses are applied to investigate how they affect magnetic phase transitions in Pd-doped FeRh

films. A combination of a $100-\mu\text{A}$ constant current (current density of $1.2 \times 10^5 \text{ A/cm}^2$) and 1-ms current pulses with a 5-s delay time are applied along the $[0\bar{1}0]$ axis, while the longitudinal voltage is recorded along the channel. Figure 3(a) plots the ρ_{xx} vs $\mu_0 H$ curves during the AFM-FM transition with an applied current ranging from 1.2×10^5 (detecting current) to $1.2 \times 10^7 \text{ A/cm}^2$. For small currents, ρ_{xx} vs $\mu_0 H$ is similar to that for $100 \mu\text{A}$ in Fig. 1(b) with the AFM-FM transition at $5.5 \rightarrow 8.5 \text{ T}$. With increasing current ($1.2 \times 10^7 \text{ A/cm}^2$), the AFM-FM transition occurs at much lower magnetic fields ($6 \rightarrow 2 \text{ T}$), as shown in Fig. 3(a). In contrast, the FM-AFM transition is nearly unchanged for various current pulses [Fig. 3(b)], changing the “first-order” magnetic phase transition to almost “second order.” The experimental geometry for Figs. 3(a) and 3(b) is shown in the inset of Fig. 3(b). A comparison of ρ_{xx} vs $\mu_0 H$ at 300 and 305 K in Fig. 3(c) indicates that both AFM-FM and FM-AFM transitions shift to a lower field direction when the temperature is increased by only 5 K.

The asymmetrical current-induced phase transitions can be attributed to three mechanisms. As displayed in the left panel of Fig. 3(d), the hysteresis of the first-order phase transition corresponds to the energy barrier for nucleation. This barrier height is lower under electronic excitation [30], which is reflected by the reduced hysteresis window of the magnetic phase transition. The second mechanism can be spin momentum transfer via flowing electrons, where the spin current will interact with local moments via s - d exchange interactions. The current will be spin-polarized when passing through the FM part of Pd-FeRh. Based on the Landau-Lifshitz-Gilbert equation, $\frac{\partial \mathbf{m}}{\partial t} = -\gamma(\mathbf{m} \times \mathbf{H}_{\text{eff}}) + \frac{\alpha_G}{M_0} (\mathbf{m} \times \frac{\partial \mathbf{m}}{\partial t}) + \sigma J[\mathbf{m} \times (\mathbf{m} \times \mathbf{p})]$, the spin current will contribute to an effective magnetic field, favoring the formation of FM states. Therefore, the magnetic phase transition loop will shift to the left side, as illustrated in the right panel of Fig. 3(d). In addition, the current-induced Joule effect will also contribute to this loop shift, as shown in Fig. 3(c). These mechanisms result in current-induced promotion of AFM-FM transitions. Magnetic states of Pd-FeRh after current pulses are directly observed with MFM in the dashed square of Fig. 2(a). Magnetic contrasts from -50° to 50° are presented in Fig. 3(e), where the light and dark regions are AFM and FM phases, respectively. The densities of current pulses are denoted below the arrow. The initial state is 6 T at 300 K, where little magnetic contrast is visible. Most of the Pd-FeRh remains in the AFM state, with a small part in the FM state. For an increasing current density of $2 \times 10^6 \text{ A/cm}^2$ to $1.2 \times 10^7 \text{ A/cm}^2$, the Pd-FeRh gradually transforms from AFM (light) to FM phases (dark). The transformation starts at $4 \times 10^6 \text{ A/cm}^2$ and is almost finished at $1.2 \times 10^7 \text{ A/cm}^2$, where only small AFM domains remain.

The Hall effect is generated by the anisotropic FM domains embedded in the AFM phases [29]. A simulated

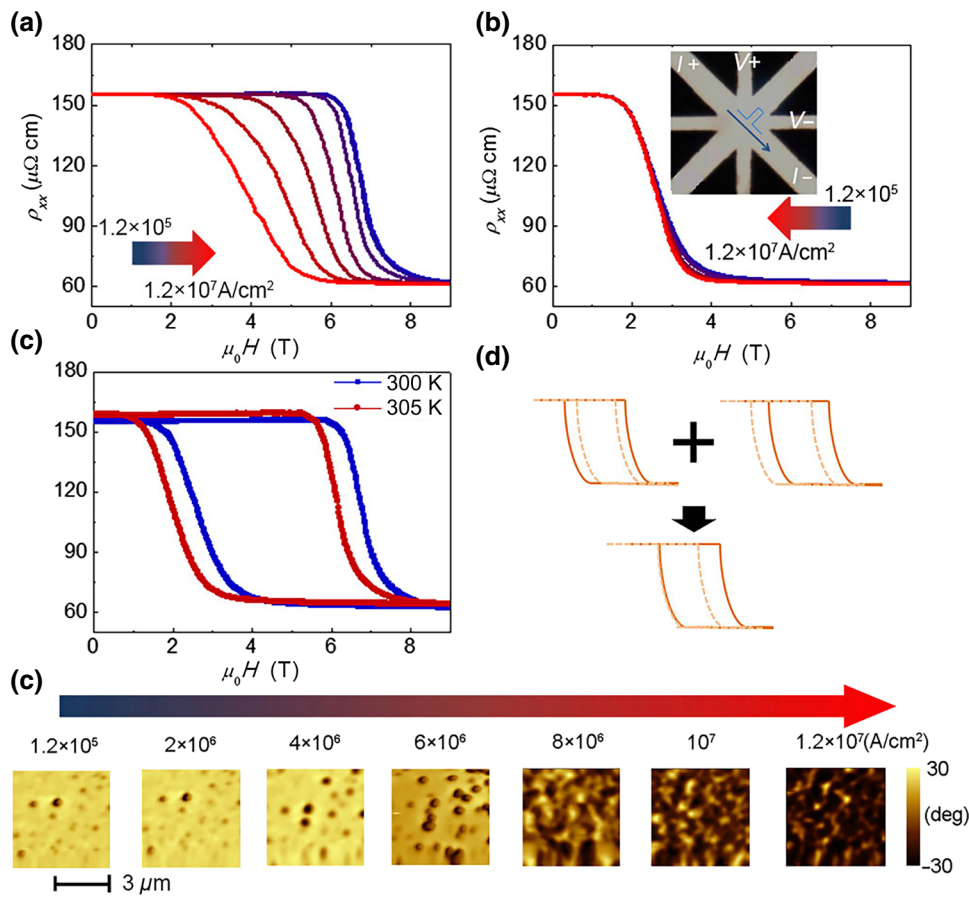


FIG. 3. (a) Resistivity vs magnetic field increases from 0 to 9 T with current pulses in different magnitudes of current density at 300 K. The width of the current pulse is 1 ms. The delay time is 5 s. The density of the current ranges from 1.2×10^5 (detecting current) to 1.2×10^7 A/cm². (b) Resistivity vs magnetic field decreases from 9 T to 0 with current pulses in different magnitudes of current density at 300 K. Inset figure shows the experimental geometry of (a) and (b). (c) The resistivity of Pd-FeRh vs magnetic field in the absence of a current pulse at 300 and 305 K. (d) Illustration of two mechanisms where current will interact with first-order magnetic phase transition. The original phase transitions are shown in solid lines while the counterparts with current excitations are shown in dotted lines. (e) MFM images are recorded at 6 T at 300 K, which serves as an initial state. Afterward, current pulses ranging from 1.2×10^5 to 1.2×10^7 A/cm² with a width of 1 ms are applied along [010] axis Pd-FeRh films, where each magnetic state after a corresponding current pulse is scanned with MFM at the identical location. The magnetic contrast is shown in the right, down panel of the figure, where the dark represents the FM and AFM is denoted in light counterpart. The scale bar is 3 μm in length.

effect of a single AFM-FM PB on the Hall signal is shown in Figs. 4(a) and 4(b), where the elliptical domains with major axes along the [010] and [100] directions are inserted into the core of the transport channel. The elliptical domain is a qualitative example with the ability of breaking symmetry to show how the anisotropy of the FM domains can affect the measured transverse voltage. The aspect ratio of the ellipse is 2.4. Because of the lower resistivity of the FM phase ($65 \mu\Omega \text{ cm}$) relative to that for the AFM phase ($155 \mu\Omega \text{ cm}$), the current at the Hall cross will mainly flow along the elliptical FM phase when the current flows along the [010] axis and [100] directions for Figs. 4(a) and 4(b). Thus, the current will be deflected to the [110] and [110] directions, respectively, as marked in the figure. It is then expected that sizeable Hall signals with opposite polarity will be obtained with

anisotropic FM domains. The diagram shows the intensity of the Hall signals, denoted by the ratio V_{xy}/V_{xx} , of transverse to longitudinal voltages, respectively. The V_{xy}/V_{xx} values in Figs. 4(a) and 4(b) are approximately 0.016 and -0.016 , respectively. The assumed distribution of electrical conductivity in the devices is plotted in Figs. 4(c) and 4(d). The embedded FM phase exhibits higher conductivity, which supports the explanation of Hall signal generation.

To determine whether the weak anisotropy of [100] PBs can be modulated by current pulses, a 100- μA constant reading current is applied along the [110] direction while the Hall voltage is recorded along the [110] direction. In addition, 1-ms current pulses with 5-s delay times are applied along the [100] axis, as illustrated in Fig. 5(a). The sign of the Hall resistivity changes

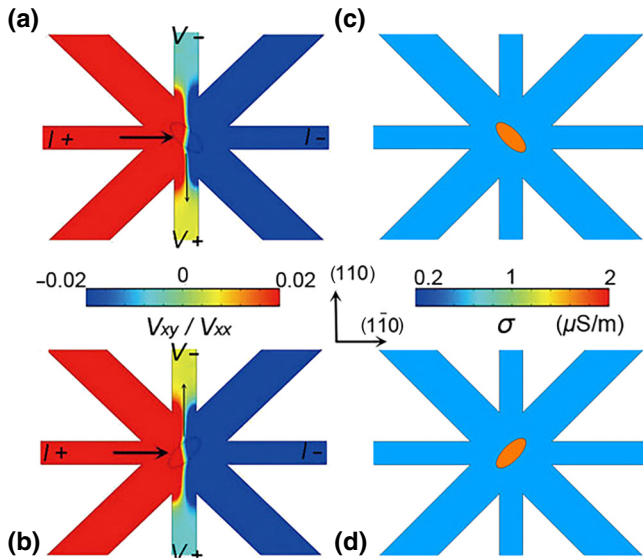


FIG. 4. (a) and (b) Simulations of Hall signal induced by anisotropic domain walls between AFM and FM along the [010] (a) and [100] (b) axis of Pd-FeRh, respectively. The V_{xy}/V_{xx} represents the ratio of transverse and longitudinal voltages. (c) and (d) The distributions of conductivity in the Hall cross corresponding to geometries of (a) and (b). σ denotes the electrical conductivity.

from negative ($-1 \mu\Omega \text{ cm}$) to positive ($1.5 \mu\Omega \text{ cm}$) with a $2 \times 10^6 \text{ A/cm}^2$ current pulse, while a higher current pulse of $8 \times 10^6 \text{ A/cm}^2$ enhances the Hall resistivity up to $9 \mu\Omega \text{ cm}$, as displayed in Fig. 5(b). This observation suggests that the anisotropy of PBs varies from the initial [100] axis to the [010] axis with the large current pulse along the [100] direction [i.e., orthogonal alignment between the PBs and the applied (writing) current]. When the current pulse is applied along the [010] direction [Fig. 5(d)], the Hall resistivity is greatly enhanced from $-1 \mu\Omega \text{ cm}$ to $-18 \mu\Omega \text{ cm}$ [Fig. 5(e)], indicating that more AFM-FM PBs nucleate and grow along the [100] axis with stronger PB anisotropy relative to the initial counterpart. The compared peak values are obtained under different magnetic fields, because the current pulse will also prompt the magnetic phase transition from AFM to FM. In contrast, the Hall signals for the FM-AFM transition are not sensitive to the current pulses, regardless of their directions along [100] [Fig. 5(c)] or [010] [Fig. 5(f)]. This asymmetric modulation is consistent with the effect of current pulses on the longitudinal resistivity (Fig. 3). Therefore, the AFM-FM PBs are formed perpendicular to the current direction, similar to the case of current-driven FM/FM or AFM/AFM DWs' motions [31–35].

IV. DISCUSSION

Electronic control of anisotropic FM domains to generate multilevel resistance is shown in Fig. 6. The

experimental configuration is identical to the scenario of Fig. 5, with a series of applied current pulses at room temperature with a fixed 4-T magnetic field [Fig. 6(a)]. The initial Hall resistivity is almost zero, indicating the AFM state of Pd-FeRh. When an $8 \times 10^6 \text{ A/cm}^2$ current pulse is applied along the [100] axis, the Hall signals have a positive sign. The Hall signals are stable over 10 consecutive current pulses, reflecting the nonvolatile nature of the anisotropic PBs. The PB state and the concomitant Hall signals can be modulated only by stronger current pulses, giving rise to multilevel resistive states. The Hall resistivity reaches a peak value of $9 \mu\Omega \text{ cm}$ with a current pulse of $1.2 \times 10^7 \text{ A/cm}^2$, as displayed in Fig. 6(b), which coincides with the positive polarity of Hall signals in Fig. 5(b). When the proportions of AFM and FM domains are comparable, a maximum of PBs are formed, resulting in the largest Hall value. With further increases in current density, more AFM domains are transformed to FM domains, resulting in fewer PBs and a decreased Hall resistivity.

The corresponding magnetic domain image in Fig. 6(d) following a current pulse of $1.2 \times 10^7 \text{ A/cm}^2$ directly supports the above conclusion, where the proportions of AFM and FM states are comparable. The PBs exhibit a main axis, for example, [010]. To semiquantitatively correlate the anisotropy of PBs and Hall signals, the Hall voltage is simulated with 2D-finite-element analysis by imprinting the PBs to the Hall cross, as shown in Fig. 6(f). The current is reflected downward, producing a positive Hall voltage, and demonstrating that the AFM-FM PBs are orientated along the [010] direction. This is consistent with the case of Fig. 4(a), which possesses a single domain with the main axis along [010]. In addition, when the current pulse is as high as $1.4 \times 10^7 \text{ A/cm}^2$, the Hall resistivity decreases because the FM FeRh domains becomes a dominant part of the films and fewer AFM-FM PBs remain. The Hall signal nearly returns to zero when the current pulse is $1.6 \times 10^7 \text{ A/cm}^2$, revealing that FeRh behaves as a FM state, accompanied by a negligible Hall effect, which is corroborated by zero Hall resistivity at both AFM and FM states in Fig. 2.

The sign of the multilevel resistive states is opposite, but the tendency is identical when the current pulse is applied along the [010] direction, as shown in Fig. 6(c). Figure 6(e) displays the MFM image after applying a current pulse of $1.2 \times 10^7 \text{ A/cm}^2$ along [010]. The domain is oriented along the [100] direction, which is supported by the 2D-finite-element analysis. The current is reflected upward, producing a negative Hall voltage, demonstrating that the AFM-FM PBs are oriented along the [100] direction, as in the case of Fig. 4(b), including a single domain with the main axis along the [100] direction. A comparison of Figs. 6(b) and 6(c) shows that the former has a smaller absolute value of the Hall resistivity ($9 \mu\Omega \text{ cm}$ vs $13 \mu\Omega \text{ cm}$). The anisotropy of the PBs can be modulated

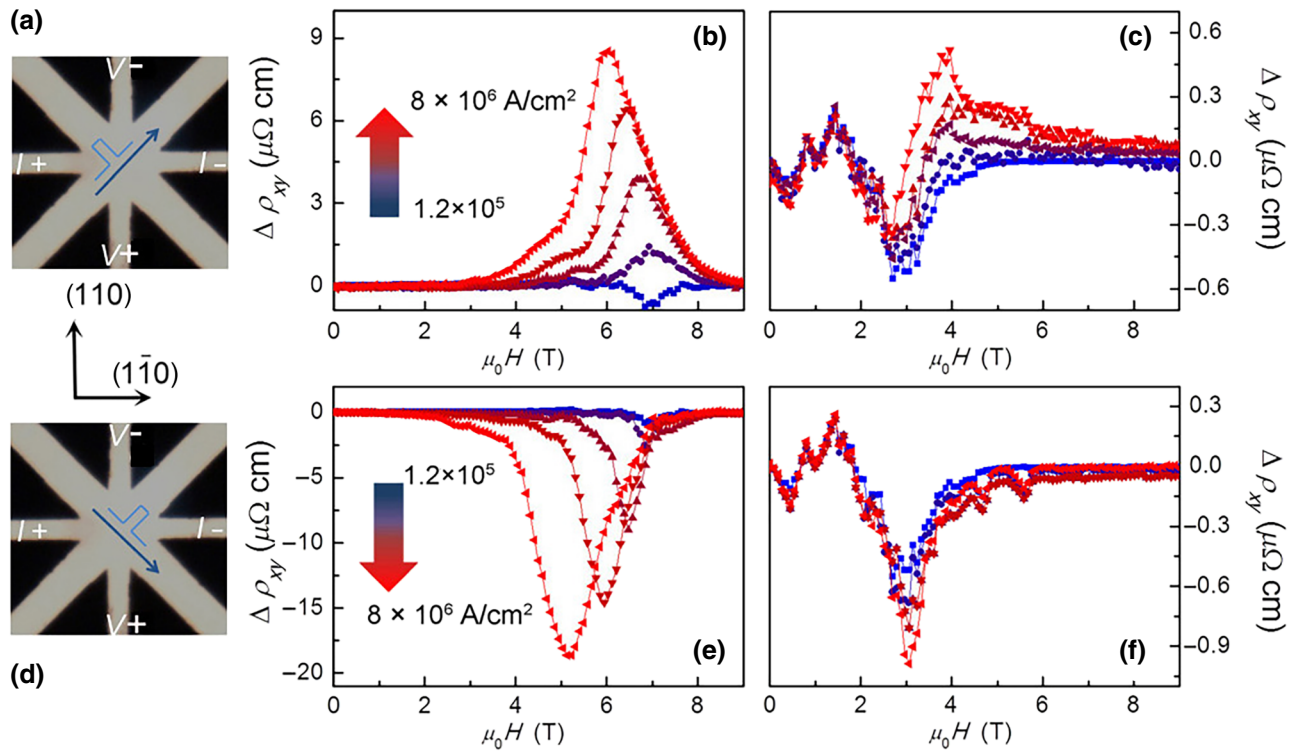


FIG. 5. (a) and (d) Schematic geometries with the current pulses along the [100] and [010] axes, respectively. The duration time of the repeated current pulses is 1 ms, while the delay time is 5 s. (b) and (e) Hall evolutions during AFM-FM phase transition. (c) and(f) Hall evolutions in FM-AFM phase transition. The current density applied in (b), (c), (e), and (f) ranges from 1.2×10^5 (detecting current) to $8 \times 10^6 \text{ A/cm}^2$. Hall signals in (b) and (c) correspond to the configuration in (a), while the curves in (e) and (f) correspond to the counterpart in (d), respectively.

along the [010] direction and become stronger with large current pulses, but it is enhanced more easily along the initial [100] axis. The 2D-finite-element analysis exhibits

a similar tendency in that the simulated value of V_{xy}/V_{xx} in Fig. 6(f) is 0.008, while the counterpart in Fig. 6(g) is -0.012 .

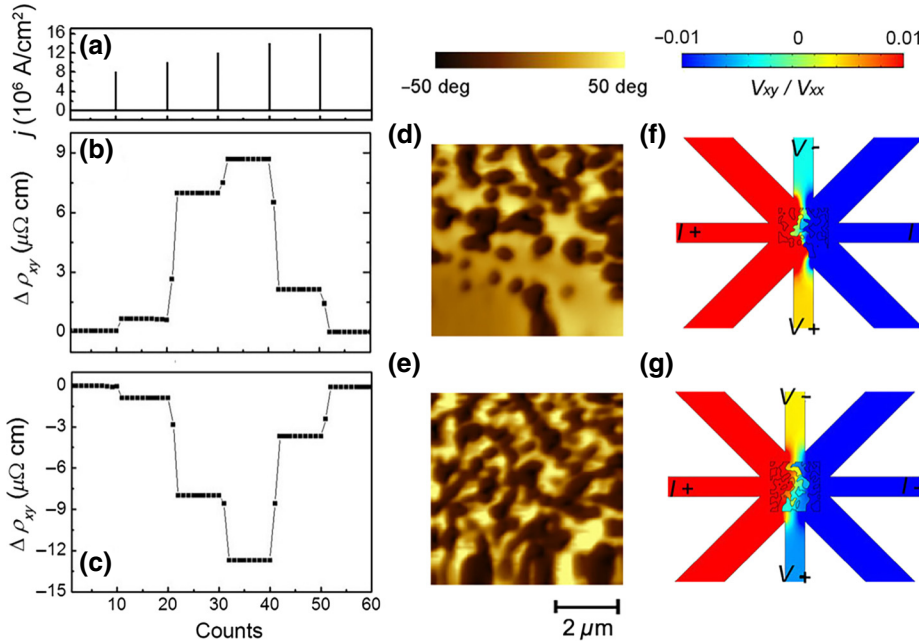


FIG. 6. (a) Current pulses with different magnitudes (only one pulse at a certain magnitude) are applied along [100] and [010] axes. The initial state is set as 4 T at 300 K. (b) and (c) Hall stages maintained after current pulses with different magnitudes in orthogonal channels along [100] (b) and [010] (c) axes. (d) and (e) MFM images after current pulse of $1.2 \times 10^7 \text{ A/cm}^2$ along [100] (d) and [010] (e) axes, respectively. (f) and (g) Simulations of Hall signals with the corresponding MFM images, which reflect the anisotropy of the domain walls. MFM images are taken at 4 T on the identical regions at 300 K. The magnetic contrasts range from -50° to 50° , while the V_{xy}/V_{xx} represents the ratio of transverse and longitudinal voltages. The scale bar is 2 μm in length.

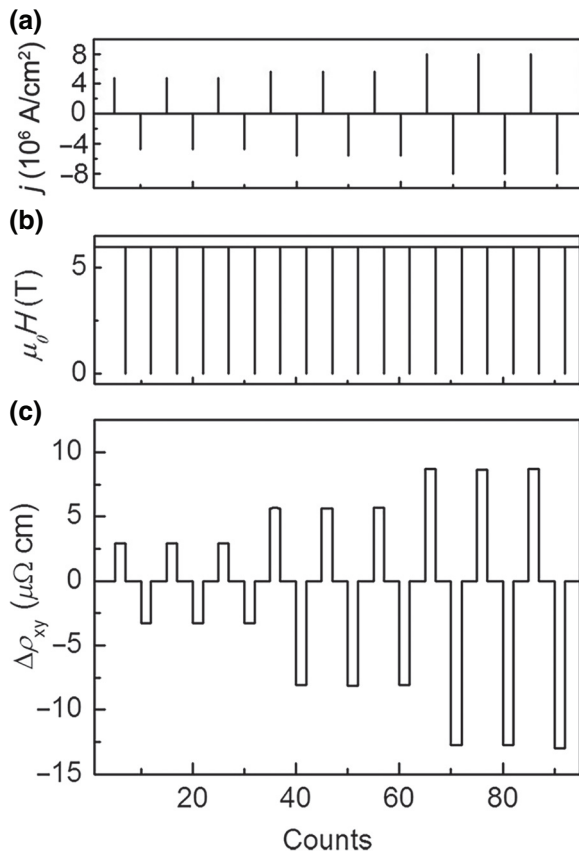


FIG. 7. Illustrations of the repeatability of the multistates Hall memory. (a) Current pulses in six different magnitudes of three periods are applied, respectively. Positive and negative magnitudes indicate applying current in the orthogonal directions along [100] and [010] axes. (b) The initial states before each current pulse are set at 6 T, 300 K. Magnetic fields are reduced from 6 T to 0 for transformation from FM to AFM states, that is, erasing the data. (c) Six repeatable Hall stages after current pulses are shown.

The reversibility of the PB anisotropies is examined by cycling the current pulses. An alternating series of $4.8 \times 10^6 \text{ A/cm}^2$, $5.6 \times 10^6 \text{ A/cm}^2$, and $8 \times 10^6 \text{ A/cm}^2$ current pulses are applied along the [100] and [010] channels. The pulses along these directions are respectively referred to as positive and negative writing signals, as illustrated in Fig. 7(a). Meanwhile, a magnetic field of 6 T is generally applied to make sure that the Pd-FeRh films remain at the AFM-FM transition state at room temperature. The required current density is lower than that used at 4 T in Fig. 5, because the increased magnetic field will reduce the AFM stability. Meanwhile, it is switched to zero field before each current pulse to erase the previous AFM-FM PBs through the FM-AFM transition [Fig. 7(b)]. With the input signals as mentioned above, typical cycling signals of the Hall resistivity are as presented in Fig. 7(c). They are recorded by the voltage measurement along the [110] direction while the reading current is applied along the

[1̄10] direction. The polarity of the Hall signals can be reversibly modulated by the alternative pulse current along the [100] and [010] directions. Hall signals with the same input current pulse (applied three times) exhibit the same polarity and magnitude, indicating the anisotropy of the PBs is highly controllable, reversible, and reproducible. Because of the enhanced PB anisotropy, the Hall signals increase with increasing current pulse (i.e., $-12 \mu\Omega \text{ cm}$ with a current pulse of $-8 \times 10^6 \text{ A/cm}^2$). The PBs between the AFM and FM domains are originally oriented along the [100] direction. Therefore, a larger current density is required to align the PBs along the [010] direction than that for alignment along the [100] direction. These controllable multilevel resistance states ensure multibit data storage based on AFM-FM PBs. In addition to the magnetic field, temperature can be used to drive the magnetic phase transition from AFM to FM, providing an opportunity for zero-field, multilevel storage encoding.

V. CONCLUSION

In conclusion, electrical control of anisotropic FM domains is realized during the magnetic phase transition of Pd-doped FeRh films. This control requires a large current pulse of 10^6 A/cm^2 , which is at the same level of current-driven magnetization switching. The AFM-FM PBs can be oriented perpendicular to the applied (writing) current, which is aligned along the [010] and [100] axes by the current pulse applied along their vertical [100] and [010] directions, respectively. The current-pulse-dependent FM-domain anisotropy produces multilevel Hall resistance in a Pd-doped FeRh Hall device. This will enable multibit data storage based on FM domains during magnetic phase transitions.

ACKNOWLEDGMENTS

We acknowledge the support of Beijing Innovation Center for Future Chip (ICFC) and Young Chang Jiang Scholars Program. This work was supported by the National Natural Science Foundation of China (Grants No. 51671110, No. 51571128, and No. 51871130) and the National Key R&D Program of China (Grant No. 2017YFB0405704).

-
- [1] S. S. P. Parkin, M. Hayashi, and L. Thomas, Magnetic domain-wall racetrack memory, *Science* **320**, 190 (2008).
 - [2] C. Chappert, A. Fert, and F. N. Van Dau, The emergence of spin electronics in data storage, *Nat. Mater.* **6**, 813 (2007).
 - [3] R. Danneau, P. Warin, J. P. Attané, I. Petej, C. Beigné, C. Fermon, O. Klein, A. Marty, F. Ott, Y. Samson, and M. Viret, Individual Domain Wall Resistance in Submicron Ferromagnetic Structures, *Phys. Rev. Lett.* **88**, 157201 (2002).

- [4] D. Buntinx, S. Brems, A. Volodin, K. Temst, and C. V. Hae-sendonck, Positive Domain Wall Resistance of Néel Walls in Co Thin Films, *Phys. Rev. Lett.* **94**, 017204 (2005).
- [5] D. Chiba, M. Yamanouchi, F. Matsukura, T. Dietl, and H. Ohno, Domain-Wall Resistance in Ferromagnetic (Ga, Mn) As, *Phys. Rev. Lett.* **96**, 096602 (2006).
- [6] X. M. Cheng, S. Urazhdin, O. Tchernyshyov, C. L. Chien, V. I. Nikitenko, A. J. Shapiro, and R. D. Shull, Antisymmetric Magnetoresistance in Magnetic Multilayers with Perpendicular Anisotropy, *Phys. Rev. Lett.* **94**, 017203 (2005).
- [7] S. Fukami, C. Zhang, S. Duttagupta, A. Kurenkov, and H. Ohno, Antisymmetric magnetoresistance in magnetic multilayers with perpendicular anisotropy, *Nat. Mater.* **15**, 535 (2016).
- [8] A. Yamaguchi, T. Ono, S. Nasu, K. Miyaka, K. Mibu, and T. Shinjo, Real-Space Observation of Current-Driven Domain Wall Motion in Submicron Magnetic Wires, *Phys. Rev. Lett.* **92**, 077205 (2004).
- [9] Y. Liu, L. C. Phillips, R. Mattana, M. Bibes, A. Barthélémy, and B. Dkhil, Large reversible calorific effect in FeRh thin films via a dual-stimulus multicaloric cycle, *Nat. Commun.* **7**, 11614 (2016).
- [10] C. Baldasseroni, C. Bordel, A. X. Gray, A. M. Kaiser, F. Kronast, J. Herrero-Albillos, C. M. Schneider, C. S. Fadley, and F. Hellman, Temperature-driven nucleation of ferromagnetic domains in FeRh thin films, *Appl. Phys. Lett.* **100**, 262401 (2012).
- [11] W. Zhang, P. K. J. Wong, D. Zhang, J. J. Yue, Z. X. Kou, G. V. D. Laan, A. Scholl, J. G. Zhang, Z. H. Lu, and Y. Zhai, Temperature-driven nucleation of ferromagnetic domains in FeRh thin films, *Adv. Funct. Mater.* **27**, 1701265 (2017).
- [12] V. Baltz, A. Manchon, M. Tsoi, T. Moriyama, T. Ono, and Y. Tserkovnyak, Antiferromagnetic spintronics, *Rev. Mod. Phys.* **90**, 015005 (2018).
- [13] C. Song, Y. F. You, X. Z. Chen, X. F. Zhou, Y. Y. Wang, and F. Pan, How to manipulate magnetic states of antiferromagnets, *Nanotechnology* **29**, 112001 (2018).
- [14] Y. Y. Wang, C. Song, B. Cui, G. Y. Wang, F. Zeng, and F. Pan, Room-Temperature Perpendicular Exchange Coupling and Tunneling Anisotropic Magnetoresistance in an Antiferromagnet-Based Tunnel Junction, *Phys. Rev. Lett.* **109**, 137201 (2012).
- [15] Z. Y. Qiu, D. Z. Hou, J. Barker, K. Sato, K. Yamamoto, O. Gomonay, and E. Saitoh, Spin colossal magnetoresistance in an antiferromagnetic insulator, *Nat. Mater.* **17**, 577 (2018).
- [16] X. Z. Chen, R. Zarzuela, J. Zhang, C. Song, X. F. Zhou, G. Y. Shi, F. Li, H. A. Zhou, W. J. Jiang, F. Pan, and Y. Tserkovnyak, Antidamping-Torque-Induced Switching in Biaxial Antiferromagnetic Insulators, *Phys. Rev. Lett.* **120**, 207204 (2018).
- [17] P. Wadley, S. Reimers, M. J. Grzybowski, C. Andrews, M. Wang, J. S. Chauhan, B. L. Gallagher, R. P. Campion, K. W. Edmonds, S. S. Dhesi, F. Maccherozzi, V. Novak, J. Wunderlich, and T. Jungwirth, Current polarity-dependent manipulation of antiferromagnetic domains, *Nat. Nanotechnol.* **13**, 362 (2018).
- [18] J. S. Kouvel and C. C. Hartelius, Anomalous magnetic moments and transformations in the ordered alloy FeRh, *J. Appl. Phys.* **33**, 1343 (1962).
- [19] J. U. Thiele, S. Maat, and E. E. Fullerton, FeRh/FePt exchange spring films for thermally assisted magnetic recording media, *Appl. Phys. Lett.* **82**, 2859 (2003).
- [20] X. Marti, et al., Room-temperature antiferromagnetic memory resistor, *Nat. Mater.* **13**, 367 (2014).
- [21] R. O. Cherifi, V. Ivanovskaya, L. C. Phillips, A. Zobelli, I. C. Infante, E. Jacquet, V. Garcia, S. Fusil, P. R. Briddon, N. Guiblin, A. Mougin, A. A. Ünal, F. Kronast, S. Valencia, B. Dkhil, A. Barthélémy, and M. Bibes, Electric-field control of magnetic order above room temperature, *Nat. Mater.* **13**, 345 (2014).
- [22] I. Suzuki, T. Naito, M. Itoh, and T. Taniyama, Barkhausen-like antiferromagnetic to ferromagnetic phase transition driven by spin polarized current, *Appl. Phys. Lett.* **107**, 082408 (2015).
- [23] M. Jiang, X. Z. Chen, X. J. Zhou, B. Cui, Y. N. Yan, H. Q. Wu, F. Pan, and C. Song, Electrochemical control of the phase transition of ultrathin FeRh films, *Appl. Phys. Lett.* **108**, 202404 (2016).
- [24] Z. Q. Liu, L. Li, Z. Gai, J. D. Clarkson, S. L. Hsu, A. T. Wong, L. S. Fan, M.-W. Lin, C. M. Rouleau, T. Z. Ward, H. N. Lee, A. S. Sefat, H. M. Christen, and R. Ramesh, Full Electroresistance Modulation in a Mixed-Phase Metallic Alloy, *Phys. Rev. Lett.* **116**, 097203 (2016).
- [25] C. J. Kinane, M. Loving, M. A. de Vries, R. Fan, T. R. Charlton, J. S. Claydon, D. A. Arena, F. Maccherozzi, S. S. Dhesi, D. Heiman, C. H. Marrows, L. H. Lewis, and S. Langridge, Observation of a temperature dependent asymmetry in the domain structure of a Pd-doped FeRh epilayer, *New J. Phys.* **16**, 113073 (2014).
- [26] X. Z. Chen, J. F. Feng, Z. C. Wang, J. Zhang, X. Y. Zhong, C. Song, L. Jin, B. Zhang, F. Li, M. Jiang, Y. Z. Tan, X. J. Zhou, G. Y. Shi, X. F. Zhou, X. D. Han, S. C. Mao, Y. H. Chen, X. F. Han, and F. Pan, Tunneling anisotropic magnetoresistance driven by magnetic phase transition, *Nat. Commun.* **8**, 449 (2017).
- [27] H. Miyajima, S. Yuasa, and Y. Otani, First-order magnetic phase transitions observed in bct FeRh–Pt, Pd systems, *Jpn. J. Appl. Phys.* **32**, 232 (1993).
- [28] Q. B. Hu, J. Li, C. C. Wang, Z. J. Zhou, Q. Q. Cao, T. J. Zhou, D. H. Wang, and Y. W. Du, Electric field tuning of magnetocaloric effect in $\text{FeRh}_{0.96}\text{Pd}_{0.04}/\text{PMN-PT}$ composite near room temperature, *Appl. Phys. Lett.* **110**, 222408 (2017).
- [29] X. Z. Chen, H. Liu, L. F. Yin, H. Chen, C. Song, and F. Pan, Hall detection of anisotropic domain walls during magnetic phase transition, *J. Phys. D: Appl. Phys.* **50**, 50 (2017).
- [30] T. Seifert, et al., Terahertz spin currents and inverse spin Hall effect in thin-film heterostructures containing complex magnetic compounds, *Spin* **7**, 1740010 (2017).
- [31] T. Shiino, S. H. Oh, P. M. Haney, S. W. Lee, G. Go, B. G. Park, and K. J. Lee, Antiferromagnetic Domain Wall Motion Driven by Spin-Orbit Torques, *Phys. Rev. Lett.* **117**, 087203 (2016).
- [32] Y. Yoshimura, K. J. Kim, T. Taniguchi, T. Tono, K. Ueda, R. Hiramatsu, T. Moriyama, K. Yamada, Y. Nakatani, and T. Ono, Soliton-like magnetic domain wall motion induced by the interfacial Dzyaloshinskii-Moriya interaction, *Nat. Phys.* **12**, 157 (2015).

- [33] T. Weindler, H. G. Bauer, R. Islinger, B. Boehm, J.-Y. Chauleau, and C. H. Back, Magnetic Damping: Domain Wall Dynamics Versus Local Ferromagnetic Resonance, *Phys. Rev. Lett.* **113**, 237204 (2014).
- [34] W. J. Jiang, P. Upadhyaya, Y. B. Fan, J. Zhao, M. S. Wang, L.-T. Chang, M. R. Lang, K. L. Wong, M. Lewis, Y.-T. Lin, J. S. Tang, S. Cherepov, X. Z. Zhou, Y. Tserkovnyak, R. N. Schwartz, and K. L. Wang, Direct Imaging of Thermally Driven Domain Wall Motion in Magnetic Insulators, *Phys. Rev. Lett.* **110**, 177202 (2013).
- [35] X. F. Zhou, J. Zhang, F. Li, X. Z. Chen, G. Y. Shi, Y. Z. Tan, Y. D. Gu, M. S. Saleem, H. Q. Wu, F. Pan, and C. Song, Strong Orientation-Dependent Spin-Orbit Torque in Thin Films of the Antiferromagnet Mn₂Au, *Phys. Rev. Appl.* **9**, 054028 (2018).